Journal of Solid State Chemistry 186 (2012) 208–216

Contents lists available at SciVerse ScienceDirect

Journal of Solid State Chemistry

journal homepage: www.elsevier.com/locate/jssc

Simultaneous pore enlargement and introduction of highly dispersed Fe active sites in MSNs for enhanced catalytic activity

Jin Lou Gu [a,*], Xu Dong [a], S.P. Elangovan [b], Yongsheng Li [a], Wenru Zhao [a], Toshio Iijima [b], Yasuo Yamazaki [b], Jian Lin Shi [a,c,**]

[a] Key Laboratory for Ultrafine Materials of Ministry of Education, School of Materials Science and Engineering, East China University of Science and Technology, Shanghai 200237, China

[b] Nippon Chemical Industries Co. Ltd., Tokyo 136-8515, Japan

[c] State Key Laboratory of High Performance Ceramics and Superfine Microstructures, Shanghai Institute of Ceramics, Chinese Academy of Sciences, Shanghai 200050, China

ARTICLE INFO

Article history:
Received 10 August 2011
Received in revised form
11 December 2011
Accepted 12 December 2011
Available online 19 December 2011

Keywords:
Nanotechnology
Mesoporous silica
Catalyst
Pore expansion
Heteroatoms

ABSTRACT

An effective post-hydrothermal treatment strategy has been developed to dope highly dispersed iron catalytical centers into the framework of mesoporous silica, to keep the particle size in nanometric scale, and in the meanwhile, to expand the pore size of the synthesized mesoporous silica nanoparticles (MSNs). Characterization techniques such as XRD, BET, SEM and TEM support that the synthesized samples are long period ordered with particles size about 100 nm and a relatively large pore size of *ca.* 3.5 nm. UV–vis, XPS and EPR measurements demonstrate that the introduced iron active centers are highly dispersed in a coordinatively unsaturated status. NH_3-TPD verifies that the acid amount of iron-doped MSNs is quite high. The synthesized nanocatalysts show an excellent catalytic performance for benzylation of benzene by benzyl chloride, and they present relatively higher yield and selectivity to diphenylmethane with a lower iron content and much shorter reaction time.

1. Introduction

Ordered mesoporous silica (OMS), which were first synthesized by scientists from Mobil [1,2], possess high surface area and tunable porous structure. They thus have attracted tremendous interest in the past decade owing to their broad applications, especially in heterogeneous catalytic processes involving large molecules [3–5]. However, for pure silica, there are few catalytically active sites on its amorphous SiO_2 framework [6] in contrast to the fact that zeolites usually possess a large number of isolated active sites [7,8]. Consequently, many successful synthetic methods have been developed to prepare mesoporous silica with isomorphous substitution of hetero-elements such as aluminum [9,10], gallium [11], titanium [12], vanadium [13], manganese [14], and iron [15–17] into silica framework for obtaining high-performance catalysts or catalyst supports.

Another issue needs to be solved is how to guarantee the full accessibility of the catalytically active centers [18]. The pore channels of the bulky OMS are generally as long as several or even tens of micrometers, the diffusion and subsequently effective collision to the active centers for reagents can become a determining factor on the efficiency of the catalytic reactions [19]. To make the introduced active centers work efficiently, a general strategy is to reduce the particle size of these bulky OMS as far as possible, e.g. down to the nanometer scale. Many efforts have been recently made to prepare this type of nanocatalyst support [20–24]. However, up to now, the pore diameter of the reported mesoporous silica nanoparticles (MSNs), which is generally templated by cetyltrimethylammonium bromide (CTAB), is as small as about 2.5 nm [25,26]. Such a relatively small pore size will also prevent the reagents with larger sizes from accessing the catalytically active centers. To some extent, this will counteract the advantages benefitting from the reduction of particle size [27]. Therefore, it is still highly desirable to prepare the nanosized mesoporous catalysts with uniformly dispersed heterogeneous atoms as catalytically active centers at the inner pore surface, and simultaneously, with enlarged pore diameters.

Currently, there are several available methods to expand the pore size of OMS [28,29], while the most commonly used technique is the introduction of a swelling agent such as trimethylbenzene (TMB) into the structure directing template, either in the preparation step [30] or in the post-hydrothermal treatment (HT) [31]. It was proposed that TMB molecules located themselves in the hydrophobic interiors of the surfactant micelles, leading to the increased

* Corresponding author. Fax: +86-21 64252599.
** Corresponding author at: Key Laboratory for Ultrafine Materials of Ministry of Education, School of Materials Science and Engineering, East China University of Science and Technology, Shanghai 200237, China. Fax: +86-21 64252599.
E-mail addresses: jinlougu@ecust.edu.cn (J.L. Gu), jlshi@mail.sic.ac.cn (J.L. Shi).

0022-4596/$ - see front matter © 2011 Elsevier Inc. All rights reserved.
doi:10.1016/j.jssc.2011.12.018

micelle diameter, and consequently the enlarged pore size of the resulting OMS. Actually, the hydrophobic region of surfactant micelle could provide the compatible environment for accommodating the hydrophobic compounds, not only for swelling agents such as pure chemical solvent of TMB, but also for some metal complexes such as hydrophobic ferric acetylacetonate ($Fe(acac)_3$), which would enhance the overall solubility of hydrophobic compounds in the hydrophobic core and prevent their aggregation [32,33]. After the *in situ* pyrolysis of the metallic precursors, the resultant metallic species can be highly dispersed within the mesopore channels since the surfactant is only encapsulated in the pore channels of OMS during the self-assembly synthesis [34]. These imply that the introduction of metallic heteroatoms into silica framework and pore expansion of OMS can be simultaneously achieved if the mixture solution of TMB and hydrophobic metallic precursors was used to serve as a swelling agent.

Generally, the reported methods for small size MSN preparation were direct sol–gel process in a heated solvent such as in water at 80 °C [35] or water–ethanol mixture at 40–50 °C without HT [36]. The average pore size of the MSN was around 2.5 nm when the cationic surfactant of CTAB was used as the structure directing agent. To expand the pore size, a swelling agent could be introduced either in the preparation step or in the post-HT [28–31]. However, the process for MSN preparation is very sensitive to the synthesis conditions. Especially, when large amount of additives such as $Fe(acac)_3$ or TMB are added to the parent solution, it will destroy the ordering structure of the obtained MSNs [37]. Additionally, since MSNs are generally prepared in strong alkaline media such as NaOH or NH_4OH aqueous solution, high concentration OH^- will inevitably attack the hydrophobic compounds such as $Fe(acac)_3$ and changes its inherent hydrophobicity to hydrophilicity, which will make the metallic compounds undissolvable in the hydrophobic cores of the surfactant [38]. Therefore, post-HT seems more suitable for the pore expanding of the synthesized MSNs using the mixture solution of TMB with $Fe(acac)_3$ dissolved. During the sol–gel process for parent MSN preparation, the morphology and the particle size have been completely controlled by a simple surfactant templated, base-catalyzed condensation procedure [35]. Then during the subsequent HT procedure without removing the surfactant from MSNs, TMB and $Fe(acac)_3$ will be co-infiltrated into the hydrophobic core of CTAB micelles as both the pore expander and iron precursor. Large pore size will be produced in the final obtained MSNs due to the expanding effect of the hydrophobic compounds and highly dispersed iron active centers will be also created upon subsequent pyrolysis.

In the present work, we report this simple post-HT method and intend to solve those three issues together, i.e. to dope the highly dispersed iron catalytically active centers into the framework of MSNs, to keep the particle size in nanometric scale and simultaneously to expand the pore size of the synthesized MSNs. We also demonstrate that the synthesized nanocatalysts show excellent catalytic performance for benzylation of benzene by benzyl chloride (BC), a very important Friedel–Crafts alkylation reactions commonly used in organic chemistry [39–42].

2. Experimental

2.1. Preparation of parent MSNs

The MSNs were synthesized using a surfactant templated, base-catalyzed condensation procedure. Specifically, CTAB (1.02 g, 2.76 mmol) was dissolved in distilled water (480 mL) along with NaOH (3.5 mL, 2 M). The solution was heated to 80 °C before adding tetraethylorthosilicate (TEOS, 5 mL). The reaction mixture was stirred for an additional 2 h at 80 °C. The white precipitate were isolated by filtration and washed with copious amount of water and ethanol. The synthesized MSNs were dried at 100 °C for *ca.* 8 h and then grinded into the powder. Thereafter the surfactant template was kept within the mesochannels of MSNs for the subsequent dissolving of the hydrophobic compounds of $Fe(acac)_3$.

2.2. Preparation of iron doped MSNs (Fe-MSNs) with large pore size

MSNs with expanded pores were prepared using silica/surfactant composite and TMB dissolved with different amount of $Fe(acac)_3$ as swelling agents under hydrothermal conditions. Specifically, dried as-synthesized MSN (1 g) was treated with distilled water (30 mL) and the mixture solution was vigorously stirred for about half an hour in an autoclave. Another portion of mixture solution was prepared by dissolving different amount of $Fe(acac)_3$ (40, 60 and 100 mg) in TMB (4 mL). Then the prepared solution was poured into the above autoclave and then heated at 120 °C for 36 h.

The resultant MSNs with large pore size and $Fe(acac)_3$ incorporated were collected by filtering the suspension. Then the samples were washed several time with distilled water and ethanol and dried at 100 °C for 24 h. The obtained powder was calcined at 600 °C for 2 h and finally, highly dispersed Fe ions doped MSNs with large pore size were prepared. According to the measured Fe content in MSNs, *viz.* 1.01, 1.52, 2.04 wt%, the corresponding samples were labeled as Fe-MSNs-1, Fe-MSNs-2 and Fe-MSNs-3 or sample 1, sample 2 and sample 3, respectively.

2.3. Characterizations

UV–vis absorption and diffuse reflectance spectra were recorded on a Shimadzu UV–vis 3101 spectroscopy. X-ray diffraction (XRD) patterns were collected with Bruker D8 using Cu $K\alpha$ radiation (40 kV, 40 mA). N_2 adsorption–desorption isotherms were obtained on NOVA 4200e at 77 K under a continuous adsorption condition. All samples were pretreated for 12 h at 393 K under nitrogen before measurements. The Brunauer–Emmett–Teller (BET) method was utilized to calculate the specific surface areas using adsorption data in a relative pressure range from 0.2 to 0.4. By using the Barrett–Joyner–Halenda (BJH) model, the pore volumes and pore size distributions were derived from the adsorption branches of isotherms, and the total pore volumes were estimated from the adsorbed amount at a relative pressure P/P_0 of 0.99. The elemental composition was determined by inductively coupled plasma atomic emission spectroscopy (ICP-AES) after the sample was dissolved in a mixture of HF and HNO_3. Transmission electron microscopy (TEM) and energy dispersive spectroscopy (EDS) was conducted on a JEM 2100F electron microscope operated at 200 kV. Field emission scanning electron microscopy (FESEM) was performed on JEOL JSM6700F electron microscope. X-ray photoelectron spectroscopy (XPS) signals were collected on a VG Micro-MK II instrument using monochromatic Mg $K\alpha$ X-rays at 1253.6 eV operated at 150 W. Calibration of the binding energies was made with the C1*s* binding energy of standard hydrocarbons (284.6 eV). Electron paramagnetic resonance (EPR) were measured at a Bruker X-band EPR spectrometer operated at a frequency of 100 kHz, microwave powder of 9.79 GHz and a time constant of 500 ms and the experiments were performed at room temperature.

2.4. Acidic and catalytic property studies

Temperature-programmed desorption of ammonia (NH_3-TPD) was performed by using a home-made apparatus. The samples (50 mg) were pretreated at 823 K for 1 h and then cooled down to

373 K under a He flow. Pure NH_3 was injected until adsorption saturation was reached, followed by a flow of He only for 30 min. Then the temperature was raised from 373 K to 873 K with a heating rate of 1 K min^{-1} and the amount of desorbed ammonia was detected by using gas chromatography.

The alkylation of benzene by BC was used as a model reaction to test the catalytic properties for the synthesized nanocatalysts. The catalytic reactions were performed under N_2 in a 50 mL three-necked flask equipped with a reflux condenser and a septum. The temperature of the reaction vessel was maintained using an oil bath. In a typical run, the prepared catalyst (0.1 g) was first activated at 673 K in air for 4 h and cooled to room temperature prior to their use in the reaction. Then the solid catalyst was introduced into reaction vessel loaded with mixed solution (27.16 mL) of benzene (25 mL) and BC (2.16 mL) (the molar ratio of benzene to BC was kept at 15). The reaction mixture was vigorously stirred and heated to the required temperature (typically 333, 343 and 353 K). Samples were withdrawn at regular intervals and analyzed using GC–MS (Agilent, 6890/5973N). Since benzene was used in excess, conversion was calculated based on the benzylating reagent of BC. The selectivity is expressed by the molar ratio of formed impurities to converted benzyl chloride. The catalyst was separated from the reaction solution by centrifugation after the first complete conversion and reused after reactivation at 873 K for 4 h. The following recycles were performed after each reaction with the same procedures. Generally, the catalytic reactions were repeated for three times to reduce the experiment errors.

3. Results and discussion

3.1. Synthetic mechanism

The synthetic protocol used here to incorporate catalytically active centers of iron into the pore channels of MSNs is shown in Fig. 1. MSNs were firstly prepared by a well reported base-catalyzed sol–gel process [35]. After filtering, washing and brief drying, all the impurities were separated and consequently no strong base ions of OH^- were left to attack the later-added iron precursor of $Fe(acac)_3$. MSNs with surfactant retained in the pore channels could maintain their nano-spherical morphology during washing and drying processes and were put into the autoclave for HT with a mixture solution of TMB and $Fe(acac)_3$. Since hydrophobic region of CTAB micelles could serve as an effective carrier for hydrophobic compounds [32], TMB and $Fe(acac)_3$ were co-infiltrated into the pore channels to expand the pore size and at the same time to introduce the iron species. Iron active centers could be highly and uniformly dispersed within silica framework due to the molecular level dissolution of the precursor compounds into the hydrophobic core of the surfactant template [34].

UV–vis spectra were used to monitor the assembly process for the encapsulation of the hydrophobic compound of $Fe(acac)_3$. The characteristic feature of the spectrum for $Fe(acac)_3$ itself dissolved in ethanol is manifested by the very strong absorption bands at about 240–300 nm due to the transition of a pi–pi* type electrons (Fig. 2b) [43]. After HT of MSNs in water solution with TMB and $Fe(acac)_3$ dissolved, it was found that almost the same peaks were present in MSNs suspension using ethanol as a solvent under the same nanoparticle concentrations. Due to the slight difference of micro-environment in the hydrophobic core of surfactant from ethanol solution, the absorption peaks for the encapsulated $Fe(acac)_3$ shift very slightly to the lower wavelength region as shown in Fig. 2 [38]. The peak intensity for samples 1, 2 and 3 (Samples 1, 2, 3 or Fe-MSNs-1, Fe-MSNs-2, Fe-MSNs-3 are defined in the experimental section) increases gradually, in agreement with the increasing amount of $Fe(acac)_3$ loading. No distinguishable absorption peak is observed in the UV–vis spectrum for pure MSNS/CTAB composite (Fig. 2a). These results demonstrate that the $Fe(acac)_3$ has been really infiltrated into the hydrophobic core of the surfactant and also verify the synthetic mechanism we proposed.

3.2. Structural characteristics and composition analysis

The small angle XRD was applied to track the ordering evolvement of MSNs and the effect of pore expansion for the parent MSNs. As depicted in Fig. 3, the well-defined and ordered structure is present for parent MSNs. The sample exhibits hexagonally ordered mesoporous structure that is characteristic of

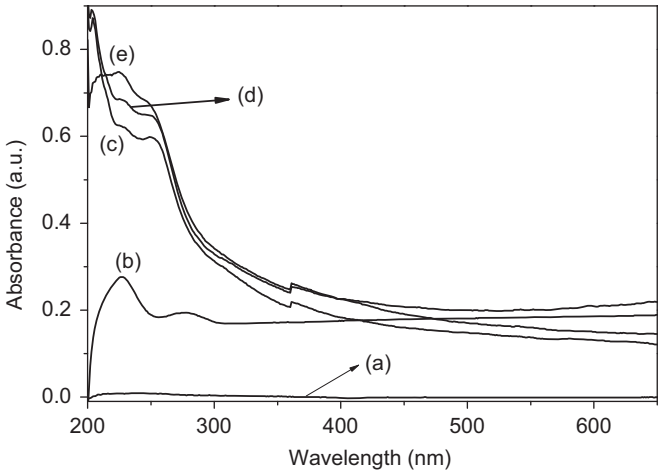

Fig. 2. UV–vis absorption spectra for parent MSNs/CTAB composite (a), fresh $Fe(acac)_3$ dissolved in ethanol solution (b), $Fe(acac)_3$ dissolved in hydrophobic inner core of CTAB surfactant micelles after hydrothermal treatment for Fe-MSNs-1 (c), Fe-MSNs-2 (d) and Fe-MSNs-3 (e).

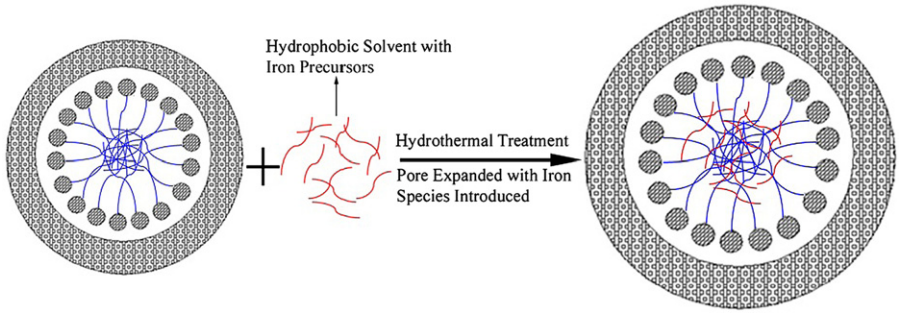

Fig. 1. Schematic illustration for incorporating the highly dispersed iron catalytically active centers into the framework of the synthesized MSNs *via* post-hydrothermal treatment with TMB and the hydrophobic iron precursors as a pore expander.

MCM-41-type with (100), (110), and (200) reflections of *p6mm* symmetry. After HT for MSNs in water/TMB mixture with $Fe(acac)_3$ dissolved, all the diffraction peaks for samples 1, 2 and 3 shift to lower angle direction, which indicates the enlarged structure units and pore sizes as we proposed. Three peaks can still be distinguished from all the samples, indicating that the structure ordering was not destroyed during HT at 120 °C for 36 h. In the wide-angle region of Fe-MSNs-3, the sample with the highest iron content, no diffraction peak (see Supporting information Fig. S1) corresponding to crystalline iron oxides could be detected. It is thus deduced that iron species were possibly doped into the framework or the particle size of iron oxides in the channels was too small to be detected by XRD.

The textural properties of Fe-MSNs with different iron amounts were characterized by nitrogen adsorption measurements. For parent MSNs, the adsorption branch shows a type IV isotherm with sharp capillary condensation steps at a relative pressure of 0.2–0.3 associated with the mesopore filling by N_2 as shown in Fig. 4a. The pore size is about 2.4 nm. This is indicative of the presence of mesoporous structure in these materials in consistent with their XRD patterns. After HT, the capillary condensation steps shift to a relative pressure of 0.4–0.55 and pore sizes are obviously expanded to about 3.5 nm for all the iron doped samples as depicted in Fig. 4. Their irreversible type IV adsorption–desorption isotherms with a H1 hysteresis loop indicate their mesoporous channels and narrow pore size distributions. These also indicate that the HT process with swelling agent and $Fe(acac)_3$ did not destroy the structure integrity of the parent MSNs. The specific pore structure along with the hexagonal unit cell parameters calculated from XRD for the synthesized samples were listed in Table 1.

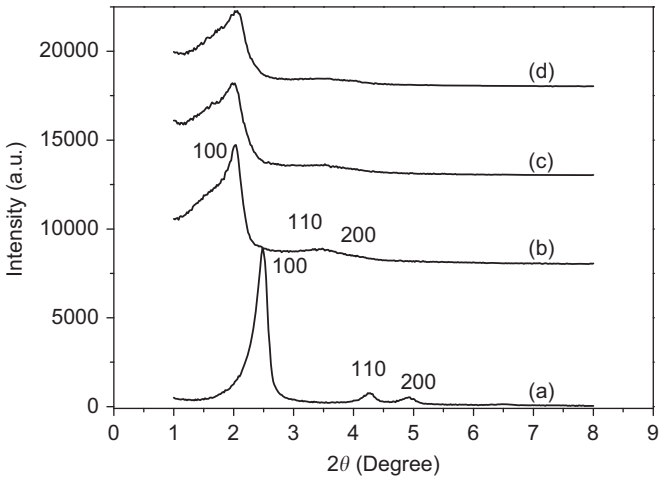

Fig. 3. Small angle XRD patterns for parent MSNs (a), Fe-MSNs-1 (b), Fe-MSNs-2 (c) and Fe-MSNs-3 (d).

It is noticeable that the specific surface areas of all the Fe-MSN samples decrease slightly but the pore volume increase significantly, which is also in agreement with the increased pore size of the iron doped samples. The relatively large pore size and almost unchanged surface area will facilitate the diffusion of reagents with a relatively large molecule [27]. In order to precisely measure the amount of iron in different samples, we also performed ICP analysis to give the specific data as shown in Table 1. We also calculated the theoretical iron contents in MSNs based on the initial composition for the nanocatalyst preparation and listed in Table 1. It was found that the iron doping efficiency achieved 90% when lower amount of iron was mixed with TMB (sample 1), while the doping efficiency decreased down to about 70% when the original $Fe(acac)_3$ concentration (TMB solution) was 25 mg/mL (we totally added 4 mL TMB into the MSN suspensions for post-HT). This suggested that the hydrophobic region of the surfactant micelle was saturated when excessive amount of iron compounds was introduced into the hydrophobic core of CTAB due to the hydrophobic affinity. Actually, no more iron species could be further introduced when we increased the initial $Fe(acac)_3$ amount above 100 mg in the current investigation.

SEM analysis was performed to investigate the final morphology of the synthesized nanocatalysts and TEM was also employed

Table 1
Pore structure parameters of the synthesized samples and the Fe contents in MSNs calculated from ICP measurements.

Samples	S_{BET} (m^2/g)	D_{BJH} (nm)	Pore volume (cm^3/g)	d_{100} (nm) [a]	a_0 (nm) [b]	Theoretical Fe (wt%) [c]	ICP Fe (wt%)
MSNs	1012	2.4	0.84	3.44	3.97	0	0
Fe-MSNs-1	912	3.5	1.19	4.21	4.86	1.12	1.01
Fe-MSNs-2	881	3.5	1.12	4.29	4.95	1.76	1.52
Fe-MSNs-3	847	3.5	1.03	4.18	4.82	2.83	2.04

[a] d_{100} was calculated from the XRD.
[b] $a_0=2d/3^{1/2}$ was the hexagonal unit cell parameter.
[c] Theoretical iron content was calculated from the initial composition for Fe-MSNs synthesis.

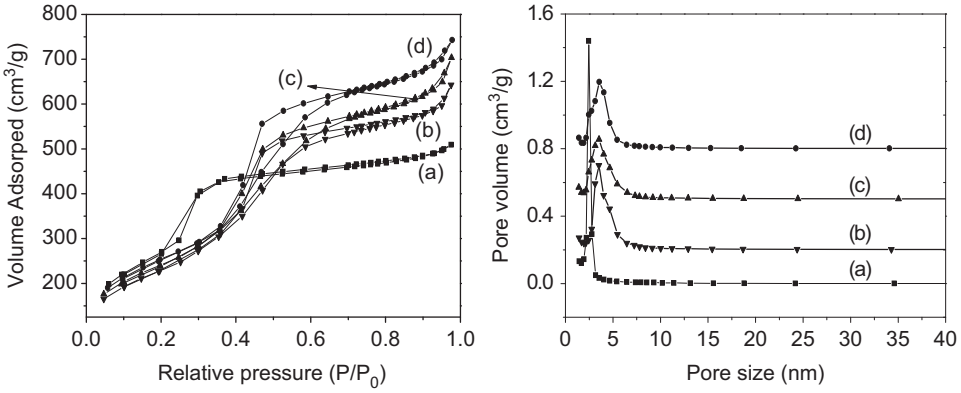

Fig. 4. The N_2 adsorption–desorption isotherms and the corresponding pore size distribution (PSD) curves for parent MSNs (a), Fe-MSNs-1 (b), Fe-MSNs-2 (c) and Fe-MSNs-3 (d).

to observe the distribution of iron species in the mesopore channels. For Fe-MSNs-1, SEM image shows that the isolated MSNs with a mean diameter of *ca.* 100 nm were obtained as shown in Fig. 5a. The particles are relatively uniform and size distribution is relatively narrow. To our knowledge, this is the first report of the MSNs with the pore diameter as large as 3.5 nm with iron active centers simultaneously incorporated in the silica framework. From TEM image of sample 1, it is clearly observed that MSNs are mainly spherically shaped. The mesopore channels are found to be basically vertical to the particle surface, which is favorable for the access of guest molecules. Mesopores with diameter of about 3.5 nm are clearly seen in the enlarged images. For Fe-MSNs-2, discrete spherical particles with a size of around 80–110 nm can be also observed from SEM image. Interestingly, the parallel pore channels also cross through the whole area of nanoparticles like sample 1 as shown in Fig. 5e. We could find some very short rod-like nanoparticles with oblate shape for Fe-MSNs-3 (Fig. 5g). The 1D hexagonal mesoporous ordering could be clearly identified from the magnified image of Fig. 5h. The pore channels are parallel to each other and along the axis direction of the short nanorods. These studies give further support that the long period ordering of the mesostructure has been largely retained in the synthesized samples after iron doping.

More importantly, no Fe_2O_3 particles can be found outside or inside the channels, even for sample 3 with the highest Fe content, which means that no aggregation or visible particles formed. Therefore, it is concluded that uniform and highly dispersed iron species were successfully introduced into the framework of silica, which benefited from the molecular level dissolution of $Fe(acac)_3$ into the hydrophobic cores of surfactant micelles. This also verifies that introduced iron active centers are highly accessible to guest molecules as the mesochannels are unblocked by introduced Fe species evidenced by the TEM images. The simultaneous EDS (see Supporting information Fig. S2) indicates that Fe signals could be detected in all synthesized nanocatalysts, and the Fe contents detected at different

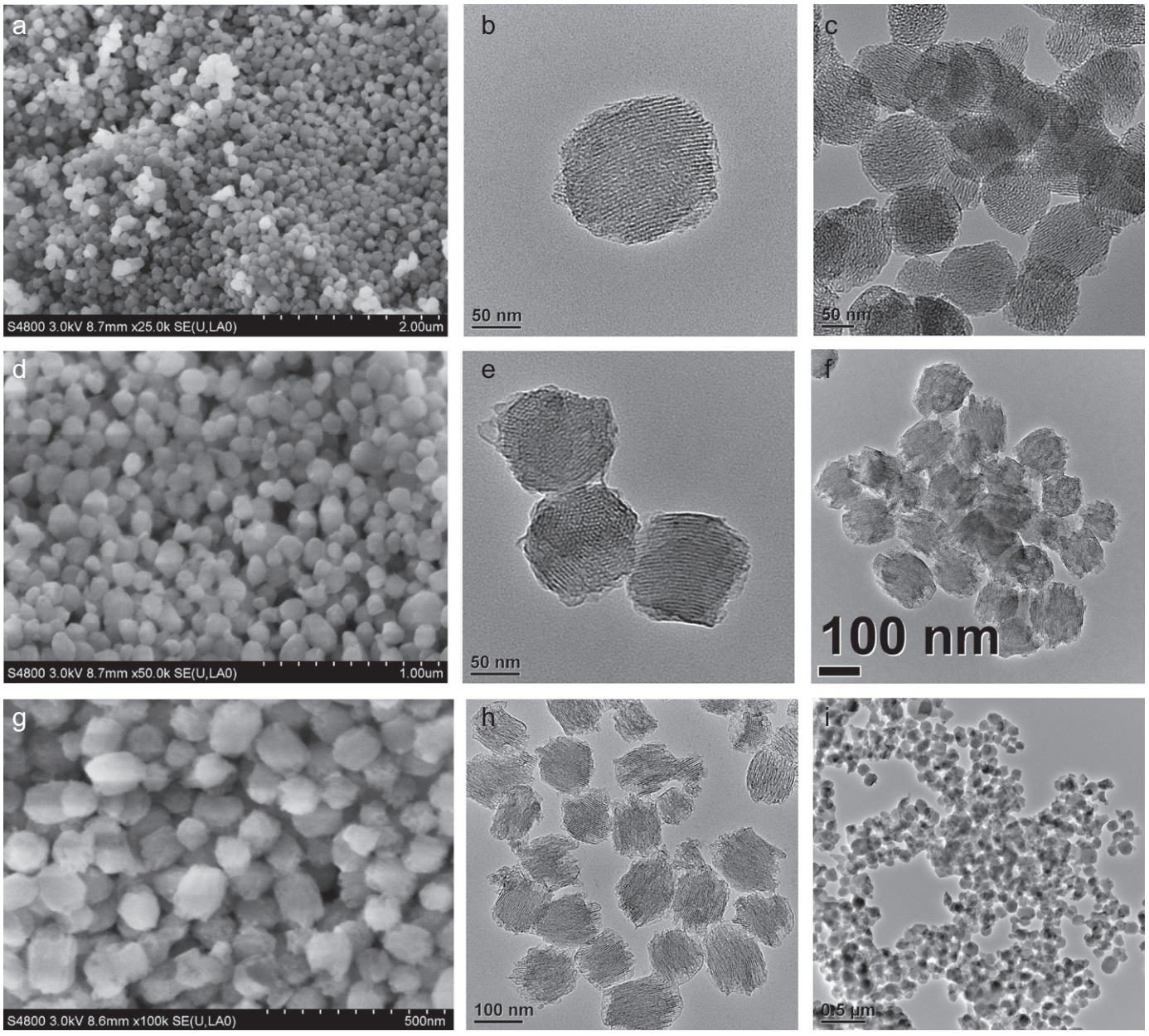

Fig. 5. Typical SEM and TEM images for the synthesized iron doped MSNs; (a), (d) and (g) are SEM images for samples 1, 2 and 3, respectively; (c), (f) and (i) are TEM images for samples 1, 2 and 3, respectively, and (b), (e) and (h) are corresponding enlarged images.

locations are almost identical to each other, which also evidences the successful and homogeneous Fe introduction and no agglomeration has been formed in agreement with the TEM observations. From the typical EDS pattern for sample 2, the corresponding Fe weight content is measured to be about 1.41 wt% in MSNs, slightly less than the value obtained from ICP.

3.3. Chemical status analysis of Fe species

UV–vis diffuse reflectance (UV–vis–DR) spectra were utilized to determine the nature and the coordination environment of iron species in different geometries. As shown in Fig. 6, no significant absorption band at or above 400 nm is observed for all the samples, even for sample 3 with iron amount *ca.* 2%, indicating that the as-synthesized nanocatalysts are free from bulk ferric oxide [44]. These further confirm the highly dispersed status of the introduced iron species in agreement with the observation of TEM images. Apparent adsorption bands below 300 nm can be clearly identified, indicating that isolated iron species does exist in all the samples, corresponding to either tetrahedral framework Fe^{3+} species or isolated extra-framework iron species in an octahedral or pseudotetrahedral environment [45]. The intensity of this absorption band increases progressively with the increasing iron content in the materials.

XPS can provide information about the elemental state in the composite materials. As clearly seen from XPS curves in Fig. 7, for all the samples, two specific peaks attributed to Fe $2p_{3/2}$ and $2p_{1/2}$ are obtained at about 712.6 and 726.6 eV, respectively, which are typical for iron(III) [46]. The signal intensity differences among samples also illustrates that the iron loading level increases progressively from sample 1 to sample 3 in agreement with ICP and UV–vis spectroscopy measurements.

To further probe the local coordination environment of iron species, EPR analysis was performed for all three samples and the recorded spectra were shown in Fig. 8. A strong signal at $g=2.0$ and a relatively weak signal at g value of 4.3 have been clearly detected for Fe-MSNs-1 and Fe-MSNs-2, while for Fe-MSNs-3, the signal peak at $g=4.3$ is almost undetectable. Such signals have often been observed for isolated iron centers incorporated into silicas, and may also be attributed to high-spin Fe^{3+} in a distorted tetrahedral environment [47]. More specifically, the signal at $g=4.3$ is typically assigned to tetrahedrally coordinated Fe^{3+} ions with strong rhombic distortion [48]. The EPR signal at $g=2.0$ is usually attributed to Fe^{3+} ions in octahedral coordination forming iron oxide clusters; meanwhile, isolated Fe^{3+} ions in positions of higher symmetry also contribute to this line [49]. For sample 1 and 2, it is inferred that iron species are in both tetrahedral coordination located in the framework and octahedral coordination forming the Fe-O-Si bond. It should be pointed out that these EPR signals were also present for iron oxide clusters [47,48]. However, we did not find Fe_2O_3 clusters in the TEM images so that this kind of coordination status could be excluded, since no Fe_2O_3 cluster were observed from TEM images. For sample 3, most iron species exist in the form of octahedral coordination forming the Fe–O–Si bond at the relatively high Fe concentration. There is no evidence for large iron oxide clusters in these samples, as these are expected to exhibit g values of 2.2–2.5 [50]. The analysis of EPR spectra combined with UV–vis spectra and TEM observations illustrate that the iron has been effectively introduced into MSNs and existed as isolated and low polymeric iron species which will subsequently serve as the active centers for the following catalysis reactions.

3.4. Acidic and catalytic property studies

The relative amount of the acid sites of the synthesized nanocatalysts were studied by NH_3-TPD since it is a useful

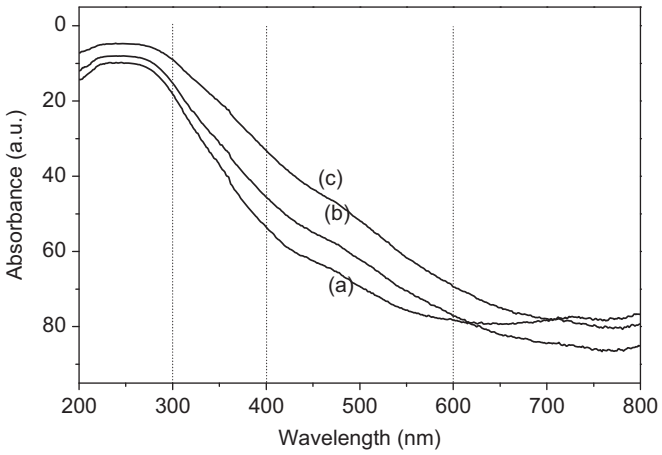

Fig. 6. UV–vis diffuse reflectance spectra of iron doped MSNs for Fe-MSNs-1 (a), Fe-MSNs-2 (b) and Fe-MSNs-3 (c).

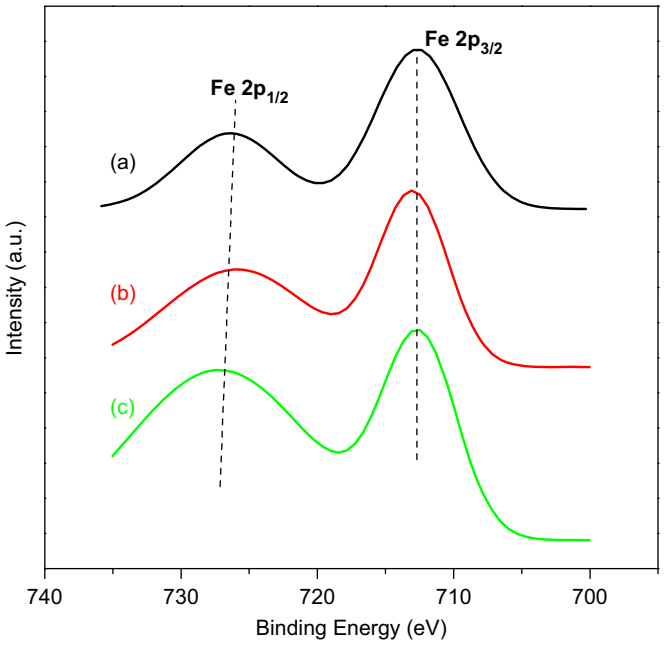

Fig. 7. XPS spectra of Fe 2*p* electrons in iron doped MSNs for sample 1 (a), sample (2) and sample (3).

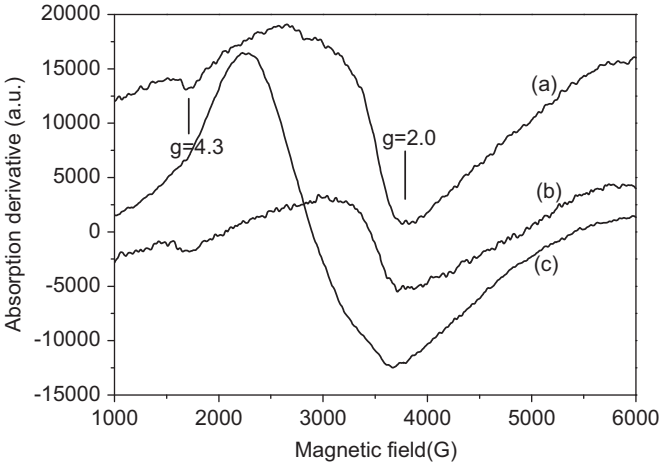

Fig. 8. EPR spectra for iron doped in the framework of MSNs of sample 1 (a), sample 2 (b) and sample 3 (c).

technique to roughly evaluate the acid strength by measuring the temperatures at which TPD peaks are observed [51]. All the NH_3-TPD profiles for iron doped MSNs are shown in Fig. 9, and the profile for pure MSNs is also shown in Fig. 9d for comparison. It can be found that there exist two broad desorption curves, the first one appears around 150 °C attributed to the weakly adsorbed ammonia and the second broad desorption peak (temperature range of 200–550 °C with a T_{max}~320 °C) is due to acidity of the samples, along with tail-like desorption at around 550 °C. Actually, since ammonia is such a strong base (pK_b is about 5) that it reacts even with extremely weak acid sites [52], therefore, we found that even for pure silica (Fig. 9d), a small NH_3 desorption peak was also present. However, the acidic site quantities of iron doped MSNs, corresponding to the total acidity [53], are much higher than that of pure MSNs. It is clearly revealed from the figures that the desorption peak intensity in the temperature range of 200–550 °C increases with the increasing iron content. The larger amount of acidity of Fe-MSNs-3 is believed to be resulted from the presence of relatively high amount of well dispersed Fe^{3+} ions in the silica framework.

The catalytic activity and selectivity of the synthesized nanocatalysts were tested for the liquid phase benzylation of benzene by BC, which holds the key importance for the production of diphenylmethane (DPM) or related compounds in pharmaceutical intermediates or fine chemical industry [39,40]. Conversion is calculated based on BC and Fig. 10 shows the conversion of BC as a function of reaction time over Fe-MSN samples under a mild reaction temperature of 333 K. It could be found that the reaction time needed for 100% conversion of BC was not longer than 60 min for all the three samples, and it decreases from 60 to 30 min with the increasing Fe loading amount, which is remarkably shorter than those reported [54]. As a control experiment, we did not detect any DPM converted from benzylation of benzene by BC over pure MSNs. These demonstrate that the Fe-MSNs are highly efficient for the current investigated catalytic reaction, and the catalytic activity is evidently increased with iron content. Although the coordination environment of Fe ions in sample 1, 2 and 3 are slightly different from each other, they all exist in a

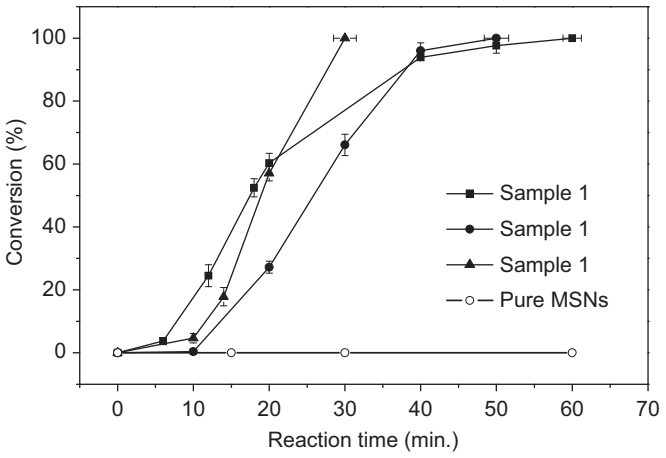

Fig. 10. Conversion of BC *vs.* reaction time on various samples with different iron loading amount at 333 K.

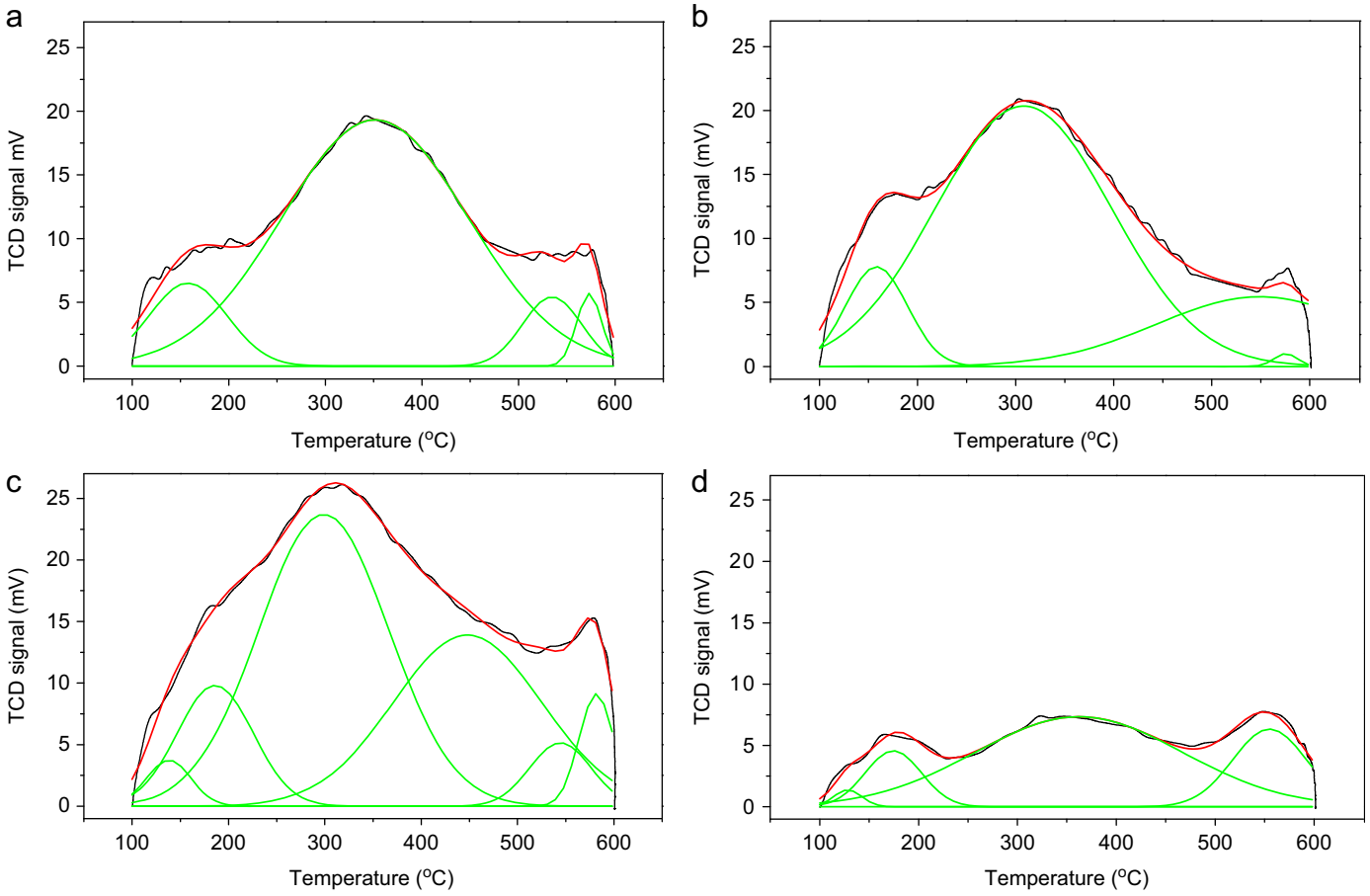

Fig. 9. NH_3-TPD curves of parent and iron doped MSNs for sample 1 (a), sample 2 (b), sample 3 (c) and parent MSNs (d). The scale for *y*-axis was set to be uniform for comparison. The red line is gauss fit for the original data and the green lines are deconvolution curves for NH_3-TPD profile. (For interpretation of the references to color in this figure legend, the reader is referred to the web version of this article.)

less coordinatively saturated status, which are highly active for the benzylaton of benzene [49,55]. This is believed to be benefitted from the intrinsic advantages of our synthetic strategy in which the molecular level dissolution and uniform distribution of the precursor compounds in the hydrophobic core of the surfactant template were achieved.

Interestingly, the selectivity to DPM is higher than 89% for all three Fe-MSN samples, and it reaches 100% for sample 3 with the highest iron content (see Supporting information Table S1). It has been reported [54] that a long reaction time of 400 min was needed to obtain complete conversion of benzyl chloride and 98.9% selectivity to DPM was achieved by using Fe-HMS as catalyst with almost the same Fe content as in our synthesized Fe-MSNs-3. Compared to those reported catalysts, our samples present higher yield of DPM and much shorter reaction time. We do believe that such a higher activity and selectivity can be attributed not only to the highly dispersed iron catalytically active centers, but also to the nanometric particle size and the enlarged pore channels of the synthesized catalysts, leading to the full accessibility of the active irons to reactant molecules.

To further evaluate the catalytic performance of sample 3, its catalytic reactivity was tested at higher temperatures to detect whether the catalytic efficiency could be further enhanced. Fig. 11 shows the effect of the reaction temperature on catalytic activity. It can be obviously found that an increase in reaction temperature gives rise to a remarkable enhancement of catalytic activity. When the temperature was set to 353 K, the reaction was rapidly completed in a very short time period of *ca.* 8 min, in sharp contrast to the 30 min duration when reacted at 333 K. The selectivity to DPM (see Supporting information Table S2) was also high, and up to 95% conversion was achieved when reacted at 353 K.

It has demonstrated in Fig. 11 that the large amount of the DPM product rapidly formed in a very short time of around 8 min when reacted at 353 K. If such a high concentration DPM molecules cannot diffuse out of mesoporous channels freely and quickly, the chemical reaction balance may be shifted, which may lead to the formation of by-product(s) and consequently the reduced selectivity, as we believe. This means that an effective way to facilitate the transport-out of the main product from the pore channels may increase the selectivity for a specific catalysis reaction. Apparently, our newly synthesized nanocatalysts with reduced particles size to nanometric scale and the expanded pore size pave the way to solve these issues.

The stability of Fe-MSNs-3 was also evaluated and the yields of the fresh and reused nanocatalyst in the benzylation of benzene

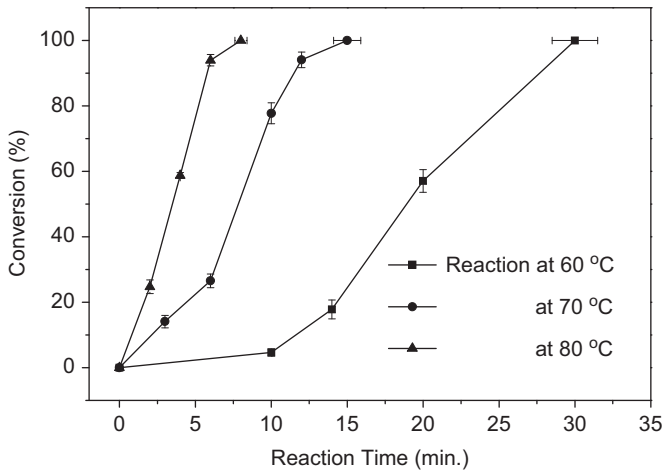

Fig. 11. Effect of reaction temperature on the conversion of BC in the benzylation of benzene over Fe-MSNs-3 nanocatalyst.

Table 2
Catalytic performance of the fresh and recycled Fe-MSNs-3 nanocatalyst in the benzylation of benzene at 343 K.

Catalyst	Time (min)	Conversation (%)	Selectivity (%)
Fresh	15	100	98.7
First reuse	15	98	95.4
Second reuse	15	94	93.7

by BC reacted at 343 K were presented in Table 2. It was found that even after three time runs, there was no significant loss in its catalytic properties, either activity or selectivity. Such catalytic characteristic is of great importance for potential industrial application. It is important to remark that the nanocatalyst has to be regenerated by recalcination to get rid of the organic species adsorbed on the catalyst surface and to maintain the activity for the successive runs.

4. Conclusions

We have developed an effective post-HT strategy to dope the highly dispersed iron active centers into the framework of MSNs, and in the meantime, the pore diameter of the synthesized MSNs was successfully expanded to *ca.* 3.5 nm, which facilitated the diffusion of the guest molecules and benefitted to the catalytic reactions involving bulky reagents. As the swelling agents worked during post-HT for the formed nanospheres, the nanoscale morphology was perfectly retained. The medium and strong acidic site quantities of Fe-MSNs were quite high and their values increased with the iron content increasing. Benefiting from the high amount of acidic sites, enlarged pore diameter and nanometric pore channel length, the synthesized nanocatalysts demonstrated high catalytic activity and selectivity for the liquid phase benzylation of benzene by benzyl chloride. It is clear that this newly developed route is general to introduce different highly dispersed metallic active centers by choosing the proper metallic precursor compounds dissolvable in TMB, and simultaneously, to expand the pore diameter. Further work will be carried out on the MSNs doping with other metal and their catalytic applications.

Acknowledgments

This work was financially supported by Shanghai Pujiang Program (no. 09PJ1403000), Research Fund for the Doctoral Program of Higher Education (no. 20090074120009), Natural Science Foundation of China (nos. 51072053, 21001043), The New Century Excellent Talents in University (no. NCET-10–0379), the Fundamental Research Funds for the Central Universities (nos. WD0911012 and WK1013001) and the Program for Changjiang Scholars and Innovative Research Team in University (Grant no. IRT0825).

Appendix A. Supplementary material

Supplementary data associated with this article can be found in the online version at doi:10.1016/j.jssc.2011.12.018.

References

[1] C.T. Kresge, M.E. Leonowicz, W.J. Roth, J.C. Vartuli, J.S. Beck, Nature 359 (1992) 710.

[2] J.S. Beck, J.C. Vartuli, W.J. Roth, M.E. Leonowicz, C.T. Kresge, K.T. Schmitt, C.T.W. Chu, D.H. Olson, E.W. Sheppard, S.B. McCullen, J.B. Higgins, J.L. Schlenker, J. Am. Chem. Soc. 114 (1992) 10834.
[3] J.M. Thomas, R. Raja, D.W. Lewis, Angew. Chem. Int. Ed. 44 (2005) 6456.
[4] S. Huh, H.T. Chen, J.W. Wiench, M. Pruski, V.S.Y. Lin, Angew. Chem. Int. Ed. 44 (2005) 1826.
[5] J.L. Gu, Y. Huang, S.P. Elangovan, Y.S. Li, W.R. Zhao, T. Iijima, Y. Yamazaki, J.L. Shi, J. Phys. Chem. C. 125 (2011) 21211.
[6] X. He, D. Antonelli, Angew. Chem. Int. Ed. 41 (2002) 214.
[7] J. Zhou, Z. Hua, J.L. Shi, Q.J. He, L.M. Guo, M.L. Ruan, Chem. Eur. J. 15 (2009) 12949.
[8] M.H. Groothaert, P.J. Smeets, B.F. Sels, P.A. Jacobs, R.A. Schoonheydt, J. Am. Chem. Soc. 127 (2005) 1394.
[9] Z.Y. Wu, H.J. Wang, T.T. Zhuang, L.B. Sun, Y.M. Wang, J.H. Zhu, Adv. Funct. Mater. 18 (2008) 82.
[10] Q.H. Yang, Y. Li, L. Zhang, J. Yang, J. Liu, C. Li, J. Phys. Chem. B 108 (2004) 7934.
[11] P. Srinivasu, A. Vinu, Chem. Eur. J. 14 (2008) 3553.
[12] F.S. Xiao, Y. Han, Y. Yu, X. Meng, M. Yang, Shuo Wu, J. Am. Chem. Soc. 124 (2002) 888.
[13] C.H. Lee, T.S. Lin, C.Y. Mou, J. Phys. Chem. B 107 (2003) 2543.
[14] A. Ramanathan, T. Archipov, R. Maheswari, U. Hanefeld, E. Roduner, R. Glaser, J. Phys. Chem. C 112 (2008) 7468.
[15] L.X. Zhang, Z.L. Hua, X.P. Dong, L. Li, H.R. Chen, J.L. Shi, J. Mol. Catal. A: Chem 268 (2007) 155.
[16] Y. Li, Y. Guan, R.A. van Santen, P.J. Kooyman, I. Dugulan, C. Li, E.J.M. Hensen, J. Phys. Chem. C 113 (2009) 21831.
[17] A.B. Bourlinos, M.A. Karakassides, D. Petridis, J. Phys. Chem. B 104 (2000) 4375.
[18] Y. Zhang, X. Shi, J.M. Kim, D. Wu, Y. Sun, S. Peng, Catal. Today 93 (2004) 615.
[19] H.T. Chen, S. Huh, J.W. Wiench, M. Pruski, V.S.-Y. Lin, J. Am. Chem. Soc. 127 (2005) 13305.
[20] K.F. Lin, P.P. Pescarmona, K. Houthoofd, D.D. Liang, G.V. Tendeloo, P.A. Jacobs, J. Catal. 263 (2009) 75.
[21] K.F. Lin, P.P. Pescarmona, H. Vandepitte, D.D. Liang, G.V. Tendeloo, P.A. Jacobs, J. Catal. 254 (2008) 254. 64.
[22] D.J. Mihalcik, W.B. Lin, Chem. Cat. Chem. 1 (2009) 406.
[23] S. Shylesh, A. Wagner, A. Seifert, S. Ernst, W.R. Thiel, Chem. Eur. J. 15 (2009) 7052.
[24] Y.F. Wang, A.V. Biradar, C.T. Duncan, T. Asefa, J. Mater. Chem. 20 (2010) 7834.
[25] G. Derrien, C. Charnay, J. Zajac, D.J. Jones, J. Roziere, Chem. Commun. (2008) 3118.
[26] D.J. Mihalcik, W.B. Lin, Angew. Chem. Int. Ed. 47 (2008) 6229.
[27] A. Sayari, D. Shee, N. Al-Yassir, Y. Yang, Top. Catal. 53 (2010) 154.
[28] M. Kruk, M. Jaroniec, A. Sayari, J. Phys. Chem. B 103 (1999) 4590.
[29] M. Mizutani, Y. Yamada, T. Nakamura, K. Yano, Chem. Mater. 20 (2008) 4777.
[30] A. Sayari, Y. Yang, M. Kruk, M. Jaroniec, J. Phys. Chem. B 103 (1999) 3651.
[31] A. Ahmed, R. Clowes, E. Willneff, H. Ritchie, P. Myers, H. Zhang, Ind. Eng. Chem. Res. 49 (2010) 602.
[32] J.L. Gu, J.L. Shi, L.M. Xiong, H.R. Chen, M.L. Ruan, Microporous Mesoporous Mater. 74 (2004) 199.
[33] J.L. Gu, J.L. Shi, L.M. Xiong, H.R. Chen, L. Li, M.L. Ruan, Solid State Sci. 6 (2004) 747.
[34] P.N. Minoofar, R. Hernandez, S. Chia, B. Dunn, J.I. Zink, A.C. Franville, J. Am. Chem. Soc. 124 (2002) 14388.
[35] C.Y. Lai, B.G. Trewyn, D.M. Jeftinija, K. Jeftinija, S. Xu, S. Jeftinija, V.S.Y. Lin, J. Am. Chem. Soc. 125 (2003) 4451.
[36] Y.S. Lin, C.P. Tsai, H.Y. Huang, C.T. Kuo, Y. Hung, D.M. Huang, Y.C. Chen, C.Y. Mou, Chem. Mater. 17 (2005) 4570.
[37] I.I. Slowing, B.G. Trewyn, V.S.Y. Lin, J. Am. Chem. Soc. 129 (2007) 8845.
[38] R.H. Holm, F.A. Cotton, J. Am. Chem. Soc. 80 (1958) 5658.
[39] H. Henti, K. Bachari, M.S. Ouali, M. Womes, B. Benaichouba, J.C. Jumas, J. Mol. Catal. A: Chem 275 (2007) 158.
[40] K. Bachari, O. Cherifi, J. Mol. Catal. A: Chem. 260 (2006) 19.
[41] Y. Sun, S. Walspurger, J.P. Tessonnier, B. Louis, J. Sommer, Appl. Catal. A—Gen. 300 (2006) 1.
[42] Y.M. Liu, J. Xu, L. He, Y. Cao, H.Y. He, D.Y. Zhao, J.H. Zhuang, K.N. Fan, J. Phys. Chem. C 112 (2008) 16575.
[43] F.D. Lewis, G.D. Salvi, D.R. Kanis, M.A. Ratner, Inorg. Chem. 32 (1993) 1251.
[44] S. Samanta, S. Giri, P.U. Sastry, N.K. Mal, A. Manna, A. Bhaumik, Ind. Eng. Chem. Res. 42 (2003) 3012.
[45] Y. Li, Z. Feng, H. Xin, F. Fan, J. Zhang, P.C.M.M. Magusin, E.J.M. Hensen, R.A. van Santen, Q. Yang, C. Li, J. Phys. Chem. B 110 (2006) 26114.
[46] A. Gervasini, C. Messi, P. Carniti, A. Ponti, N. Ravasio, F. Zaccheria, J. Catal. 262 (2009) 224.
[47] H. Liu, G. Lu, Y. Guo, Y. Guo, J. Wang, Nanotechnology 17 (2006) 997.
[48] H.C. Xin, J. Liu, F.T. Fan, Z.C. Feng, G.Q. Jia, Q.H. Yang, C. Li, Microporous Mesoporous Mater. 113 (2008) 231.
[49] K. Bachari, J.M.M. Millet, P. Bonville, O. Cherifi, F. Figueras, J. Catal. 249 (2007) 52.
[50] C. Nozaki, C.G. Lugmair, A.T. Bell, T.D. Tilley, J. Am. Chem. Soc. 124 (2002) 13194.
[51] M. Casagrande, L. Storaro, M. Lenarda, J. Gersich, L. Stievano, F.E. Wagner, T. Montanarid, J. Mater. Chem. 14 (2004) 1010.
[52] L. Chmielarz, P. Kustrowski, R. Dziembaj, P. Cool, E.F. Vansant, Appl. Catal. B: Environ. 62 (2006) 369.
[53] H. Landmesser, H. Kosslick, U. Kurschner, R. Fricke, J. Chem. Soc., Faraday Trans. 94 (1998) 971.
[54] K. Bachari, J.M.M. Millet, B. Benaichouba, O. Cherifi, F. Figueras, J. Catal. 221 (2004) 55.
[55] X.X. Wang, Y. Wang, Q.H. Tang, Q. Guo, Q.H. Zhang, H.L. Wan, J. Catal. 217 (2003) 457.